Spectroscopic and asteroseismic analysis of the remarkable main-sequence A star KIC 11145123

Masahide Takada-Hidai,[1]⋆† Donald W. Kurtz,[2]⋆ Hiromoto Shibahashi,[3]⋆ Simon J. Murphy,[4,5]⋆ Masao Takata,[3] Hideyuki Saio[6] and Takashi Sekii[7]

[1]*Liberal Arts Education Center, Tokai University, Kitakaname, Hirastuka, Kanagawa 259-1292, Japan*
[2]*Jeremiah Horrocks Institute, University of Central Lancashire, Preston PR1 2HE, UK*
[3]*Department of Astronomy, School of Science, The University of Tokyo, Bunkyo-ku, Tokyo 113-0033, Japan*
[4]*Sydney Institute for Astronomy, School of Physics, The University of Sydney, NSW 2006, Australia*
[5]*Stellar Astrophysics Centre, Department of Physics and Astronomy, Aarhus University, DK-8000 Aarhus C, Denmark*
[6]*Astronomical Institute, Graduate School of Science, Tohoku University, Sendai 980-8578, Japan*
[7]*National Astronomical Observatory of Japan, 2-21-1 Osawa, Mitaka, Tokyo 181-8588, Japan*

ABSTRACT

A spectroscopic analysis was carried out to clarify the properties of KIC 11145123 – the first main-sequence star with a directly measured core-to-surface rotation profile – based on spectra observed with the High Dispersion Spectrograph (HDS) of the Subaru telescope. The atmospheric parameters ($T_{\rm eff} = 7600$ K, $\log g = 4.2$, $\xi = 3.1$ km s^{-1} and [Fe/H] $= -0.71$ dex), the radial and rotation velocities, and elemental abundances were obtained by analysing line strengths and fitting line profiles, which were calculated with a 1D LTE model atmosphere. The main properties of KIC 11145123 are: (1) a low [Fe/H] $= -0.71 \pm 0.11$ dex and a high radial velocity of -135.4 ± 0.2 km s^{-1}. These are remarkable among late-A stars. Our best asteroseismic models with this low [Fe/H] have slightly high helium abundance and low masses of 1.4 M$_\odot$. All of these results strongly suggest that KIC 11145123 is a Population II blue straggler; (2) the projected rotation velocity confirms the asteroseismically predicted slow rotation of the star; (3) comparisons of abundance patterns between KIC 11145123 and Am, Ap, and blue stragglers show that KIC 11145123 is neither an Am star nor an Ap star, but has abundances consistent with a blue straggler. We conclude that the remarkably long 100-d rotation period of this star is a consequence of it being a blue straggler, but both pathways for the formation of blue stragglers – merger and mass loss in a binary system – pose difficulties for our understanding of the exceedingly slow rotation. In particular, we show that there is no evidence of any secondary companion star, and we put stringent limits on the possible mass of any such purported companion through the phase modulation technique.

Key words: techniques: spectroscopic – stars: abundances – stars: atmospheres – stars: individual: KIC 11145123 – stars: oscillations – stars: rotation.

1 INTRODUCTION

The *Kepler* mission provided photometry of unprecedented precision from which the core-to-surface rotation rate of a main-sequence star was measured for the first time in a model-independent manner (Kurtz et al. 2014). The A-type star, KIC 11145123, pulsates in g

modes that are sensitive to the outer core, and p modes that are sensitive to the near-surface conditions. Both types of pulsation modes show rotational splitting, from which Kurtz et al. (2014) inferred nearly rigid rotation with a period near 100 d, and, surprisingly, with the surface rotating slightly, but significantly, faster than the core. Gizon et al. (2016) then used the data of Kurtz et al. (2014) to find differences in the splitting in the frequencies of the quadrupole p modes in this star that led to the discovery that the star is *less* oblate than expected, even for such a slow rotator. Gizon et al. (2016) speculated that a magnetic field may have suppressed some of the rotational oblateness, and they announced the star as 'the roundest object in the Universe'. Since the work of Kurtz et al. (2014), similar analyses have been carried out for other A/F stars (Saio et al.

⋆ E-mail: mth_tsc@tsc.u-tokai.ac.jp (MT); dwkurtz@uclan.ac.uk (DWK); shibahashi@astron.s.u-tokyo.ac.jp (HS); simon.murphy@sydney.edu.au (SJM)
† Based on data collected at the Subaru telescope, which is operated by the National Astronomical Observatory of Japan.

2015; Murphy et al. 2016; Schmid & Aerts 2016), each showing near-uniform core-to-surface rotation in stars near the terminal age main-sequence (TAMS).

The results of those papers suggest that if A–F stars typically rotate nearly rigidly at the end of main sequence, a strong angular momentum transport mechanism must operate during the main-sequence evolution to produce such rigid rotation, and a mechanism such as internal gravity waves or mass accretion must exist to accelerate the rotation rate of the surface beyond that of the core.

The rotation period of KIC 11145123 is exceptionally long for a late-A star, and an explanation is needed for this slow rotation, along with the unexpected rigid rotation. Kurtz et al. (2014) posited some explanations and ruled out the possibility that the star is a magnetic Ap star because no known Ap star shows both g modes and low overtone p modes. They also rejected the possibility that the star is in a binary system synchronously rotating with an orbital period of 100 d, using the frequency modulation (FM) technique (Shibahashi & Kurtz 2012). Instead, they suggested that the star could be either an Am star or a blue straggler, because all Am stars and many blue stragglers are known to rotate slowly (e.g. Glaspey, Pritchet & Stetson 1994; Lovisi et al. 2013a,b).

To investigate their suggestion and clarify the properties of KIC 11145123, we performed a spectroscopic analysis of this star based on high-dispersion spectra obtained with the Subaru telescope. We also found new asteroseismic models based on our improved knowledge of the star's fundamental parameters and abundances. We find from the abundances and space velocity that the star is Population II, and our asteroseismic analysis requires some mass loss during the lifetime of the star, hence is consistent with the slow rotation. A remaining puzzle is the mechanism of that mass loss, since we are able to constrain any possible companion to sub-stellar mass, hence the star is not currently in a suitable binary to explain its earlier mass loss.

2 SPECTROSCOPIC OBSERVATIONS AND DATA REDUCTION

Our target, KIC 11145123, was observed with the High Dispersion Spectrograph (HDS; Noguchi et al. 2002) on the Subaru telescope on 2015 July 3. Echelle spectra were obtained in a standard StdYc setup covering the wavelength range of 4390–7120 Å, and using the image slicer #3 with 1×1 binning, which yields a wavelength resolution of 160 000. Four spectra were obtained, each with an exposure time of 2000 s, yielding a total exposure time of 8000 s. Basic data and the derived atmospheric parameters for our target are shown in Table 1, along with the parameters of our best asteroseismic model derived in Section 6.

Standard data reduction procedures (bias subtraction, background subtraction, cosmic ray removal, flat-fielding, extraction of 1D spectra, wavelength calibration, co-addition of spectra, combination into a single spectrum and normalization) were carried out with the IRAF échelle package.[1] The resultant spectra consist of a blue part with wavelength coverage of 4400–5720 Å, and a red part with 5800–7120 Å. Signal-to-noise ratios (S/N) were measured on peak continua of each order, and found for both blue and red parts to be 100–120. To make a Doppler correction, the radial velocity was

Table 1. Fundamental data and model parameters of KIC 11145123.

Right ascension (J2000.0)	$19^{\rm h}41^{\rm m}25^{\rm s}$
Declination (J2000.0)	$+48°45'15''$
Kp (mag)*	13.123
Spectroscopically derived parameters	
$T_{\rm eff}$ (K)	7590^{+80}_{-140}
$\log g$ (cgs)	4.22 ± 0.13
ξ (km s^{-1})	3.1 ± 0.5
[Fe/H]	-0.71 ± 0.11
$V_{\rm h}$ (km s^{-1})	-135.4 ± 0.2
Asteroseismically derived parameters	
M (mass)	$1.4\,{\rm M_\odot}$
X (H fraction)	0.70
Y (He fraction)	0.297
Z (metal fraction)	0.003

*Kp is the white light *Kepler* magnitude taken from the revised KIC (Huber et al. 2014).

measured using 64 Fe I and 24 Fe II lines. The radial velocity averaged with weights of line numbers is $V_{\rm r} = -145.4 \pm 0.2$ km s^{-1}, giving a heliocentric radial velocity of $V_{\rm h} = -135.4 \pm 0.2$ km s^{-1}, as listed in Table 1.

3 ATMOSPHERIC PARAMETERS

The parameters of the atmospheric model of our target, effective temperature ($T_{\rm eff}$), surface gravity ($\log g$), microturbulence (ξ) and metallicity ([Fe/H]),[2] were determined by following the principle and algorithm of iteration procedures described in Takeda, Ohkubo & Sadakane (2002). Their iteration procedures are based on the equivalent widths (W_λ) and abundances determined from each of the selected Fe I and Fe II lines, and find a final solution for the atmospheric parameters in the ($T_{\rm eff}$, $\log g$, ξ) parameter space by adjusting the three parameters from their initial values by small amounts. Each perturbation also results in a new [Fe/H].

In this procedure we selected 67 Fe I and 15 Fe II lines from Westin et al. (2000), and also six Fe II lines from Takeda et al. (2005). The gf-values of these Fe lines were also adopted from these sources. To analyse the Fe lines, we used the SPTOOL software package developed by Y. Takeda,[3] which is based on Kurucz's ATLAS9 1D LTE model atmospheres and WIDTH9 program for abundance analysis (Kurucz 1993). The program SPSHOW was used to measure W_λ by Gaussian profile fitting in most cases, but by direct integration in others, and the program WIDTH was used to derive abundances from the W_λ of selected Fe lines. The selected lines of Fe I and Fe II are given in Appendix A in Tables A1 and A2 along with the atomic constants and measured equivalent widths.

We obtained our solution for the atmospheric parameters using a standard iterative method as follows. We began with atmospheric parameters for our starting model selected from the *Kepler* Input Catalogue (KIC) as revised by Huber et al. (2014). At each iteration we initially kept $T_{\rm eff}$ and $\log g$ fixed, and determined ξ by insisting that the abundances derived from the Fe I lines were independent of the corresponding W_λ. This resulted in a new [Fe/H] that was used to determine $T_{\rm eff}$ under the requirement of excitation equilibrium, which specifies that the Fe I abundances are independent of the

---

[1] IRAF is distributed by the National Optical Astronomy Observatory, which is operated by the Association of Universities for Research in Astronomy, Inc., under cooperative agreement with the National Science Foundation.

[2] $[X/Y] \equiv \log (X/Y)_{\rm star} - \log (X/Y)_\odot$ is used throughout the paper.
[3] http://optik2.mtk.nao.ac.jp/takeda/sptool/

lower excitation potential, χ. The final step in the iteration was to evaluate $\log g$ under the requirement of ionization equilibrium, such that the Fe abundance derived from Fe I and Fe II lines are equal. The next iteration used the parameters thus obtained as the new starting model, until convergence was reached. The best-fitting parameters are: $T_{\rm eff} = 7590^{+80}_{-140}$ K, $\log g = 4.22 \pm 0.13$, $\xi = 3.1 \pm 0.5$ km s^{-1} and [Fe/H] $= -0.71 \pm 0.11$.

As a check of these parameters, we calculated the reduced chi-squared statistic, χ_r^2, for 16 models created from the four parameters perturbed by their uncertainties. We adopted the set of observed W_λ of 67 Fe I and 21 Fe II lines from Tables A1 and A2, and calculated W_λ of each line for each model with 88 degrees of freedom. None of those 16 models had χ_r^2 lower than that of the best-fitting model, for which we found $\chi_r^2 = 3.20$.

4 ROTATION VELOCITY

The exceptionally long rotation period near 100 d of KIC 11145123 derived asteroseismically by Kurtz et al. (2014) to predict a surface equatorial rotation velocity of $v_{\rm eq} = 1$ km s^{-1}, implying $v \sin i \leq 1$ km s^{-1}. However, observational measures of $v \sin i$ are made from line broadening, which includes macroturbulent broadening, as well as pulsational broadening from both the p modes and the g modes in this star. These additional broadening mechanisms are discussed, modelled and evaluated by Murphy et al. (2016) in the context of another relatively slowly rotating γ Dor star, KIC 7661054, where they find that the combination of the pulsational and macroturbulent broadening is of the order of several km s^{-1}, and certainly less than a total of 10 km s^{-1}. It is common usage to give the line broadening measurement as if it were only $v \sin i$, and this is a good approximation for moderate to fast rotating stars. However, when the equatorial rotation velocity is of the order of a few km s^{-1}, then it is necessary to be aware that the line broadening originates from these multiple sources.

A-type stars with normal abundances in general rotate relatively fast, with $v \sin i > 100$ km s^{-1}. Even the chemically peculiar Ap and Am stars, which generally have $v \sin i < 100$ km s^{-1}, still often show equatorial rotation velocities of tens of km s^{-1}. Thus, the asteroseismic prediction that the total line broadening from rotation, pulsation and macroturbulence of $v \sin i \leq 10$ km s^{-1} for KIC 11145123 is a strong prediction that is easily falsified, should it be incorrect – in particular, should the rotation period be significantly less than the 100 d measured asteroseismically by Kurtz et al. (2014). Therefore, to test for the predicted slow rotation of our target, we performed line profile fitting to derive the convolved line broadening velocities.

The line profile fittings were made based on the final model atmosphere, using the program MPFIT in the SPTOOL software package under the following assumptions as described by Takeda, Sato & Murata (2008):

(1) The observed spectrum is a convolution of the modelled intrinsic spectrum and the total macrobroadening function, $f_{\rm T}$.

(2) $f_{\rm T}$ is a convolution of three functions: the instrumental broadening $f_{\rm i}$; the projected rotation broadening, $f_{\rm r}$; and the macroturbulence broadening (which includes the pulsational broadening), $f_{\rm m}$. Thus, $f_{\rm T} = f_{\rm i} * f_{\rm r} * f_{\rm m}$ (* denotes convolution).

(3) We approximate these broadening functions with the same Gaussian form, parametrized by the e-folding half-width (v_k) as $f_k \propto \exp(-v^2/v_k^2)$, where k represents any of the suffixes. These broadening parameters are thus related as $v_{\rm T}^2 \equiv v_{\rm i}^2 + v_{\rm r}^2 + v_{\rm m}^2$.

Table 2. The measured values of $v_{\rm T}$ and $v_{\rm rm}$ for four lines derived from the observed spectrum of our target, KIC 11145123. The lines are listed in order of increasing W_λ, making the correlation between W_λ and $v_{\rm rm}$ obvious.

Line	W_λ mÅ	$v_{\rm T}$ km s^{-1}	$v_{\rm rm}$ km s^{-1}
Fe I 4637	17.8	6.00	5.89 ± 1.15
Cr II 4554	33.0	6.69	6.59 ± 0.43
Cr II 4634	42.0	6.75	6.66 ± 0.33
Ti II 4563	174.2	7.54	7.45 ± 0.07

(4) The combined broadening function, $f_{\rm rm}$, of the projected rotation broadening and macroturbulence broadening functions is defined as $f_{\rm rm} \equiv f_{\rm r} * f_{\rm m}$, together with the relation of the combined broadening parameter, $v_{\rm rm} \equiv \sqrt{v_{\rm T}^2 - v_{\rm i}^2} = \sqrt{v_{\rm r}^2 + v_{\rm m}^2}$.

The instrumental broadening was estimated to be $v_{\rm i} = c_0/(2\sqrt{\ln 2} R) = 1.13$ km s^{-1}, where c_0 is the speed of light and R the spectral resolution (160 000), which is derived from measurements of the full width at half-maximum of emission lines of the Th–Ar comparison spectrum.

4.1 Confirmation of an argument by Landstreet et al. (2009)

To confirm the validity of our fitting procedure to obtain $v_{\rm T}$ and $v_{\rm rm}$, we first made a test calculation for the lines studied by Landstreet et al. (2009) to test in KIC 11145123 their argument that for stars with $T_{\rm eff}$ less than about 10 000 K, $v \sin i$ is dependent on line strengths, W_λ, so that the signatures of local velocity fields may become more evident in stronger lines.

They used 10 selected lines of Cr II, Ti II, Fe I and Fe II to investigate the atmospheric velocity fields in a sample of sharp-lined main-sequence A stars. They found eight main-sequence A stars with $T_{\rm eff} < 10 000$ K in which evidence of velocity fields is directly detected in line profiles showing depressed blue wings and a discrepancy between observed and theoretical line shapes (see their table 2). Among these A stars, $v \sin i$ values were also estimated; they found that the measured $v \sin i$ is smaller when derived from weak lines than from strong lines, indicating a dependence of $v \sin i$ on line strengths. They speculated that velocity fields are probably convective motions reaching the atmosphere.

To confirm the dependence of $v \sin i$ on line strengths, we adopted four lines (Cr II 4554.99 Å and 4634.07 Å, Ti II 4563.76 Å and Fe I 4637.50 Å) used by Landstreet et al. (2009), and measured W_λ of these lines in the observed spectrum of our target. The values of $v_{\rm T}$ and $v_{\rm rm}$ were derived from profile fittings to these lines, based on the atmospheric model of our target. The gf values of these lines were adopted from Castelli & Hubrig (2004). The uncertainties of $v_{\rm rm}$ were estimated from the simulations of profile fittings to each line for several values of $v_{\rm T}$.

The results are shown in Table 2, where the values of $v_{\rm rm}$ are noticeably dependent on W_λ, indicating that $v \sin i$ depends on line strengths as argued by Landstreet et al. (2009). Because our target has $T_{\rm eff} = 7590^{+80}_{-140}$ K, the comparison with the sample in Landstreet et al. (2009) is valid. Consequently, we verified our fitting procedure and arrived at the conclusion that $v_{\rm rm}$, corresponding to $v \sin i$, is least influenced by local velocity fields in the weak line limit as $W_\lambda \to 0$ mÅ.
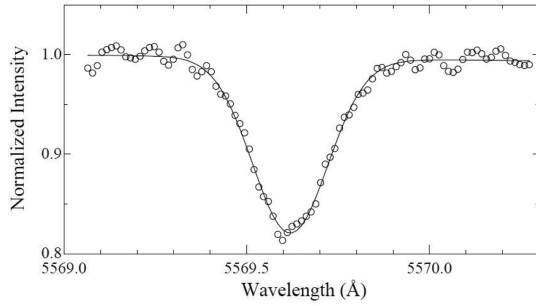
Figure 1. An example of the typical profile fitting for the Fe I 5569 Å line with $W_\lambda = 44.4$ mÅ. Open circles are the observations; the solid line shows the theoretical profile converged after five iterations. The converged solution gives $v_T = 6.7$ km s^{-1} and $v_{rm} = 6.6$ km s^{-1}, and also the abundance of log Fe I = 6.73.
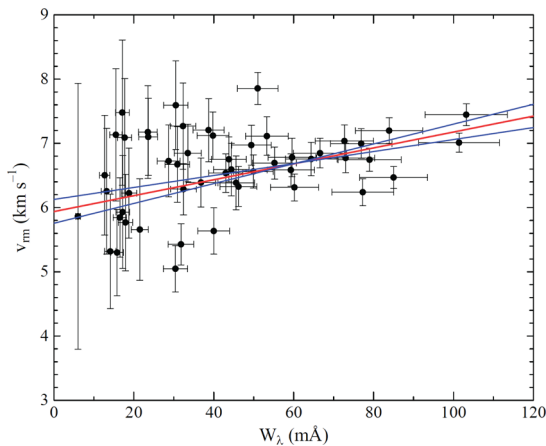
Figure 2. The values of v_{rm} derived from 51 Fe I lines are plotted as a function of W_λ together with the error bars of both W_λ (assuming a 10 per cent error) and v_{rm}. A least-squares fit is derived taking these error bars into account. The best fit is depicted in a red line with the intercept of 5.94 km s^{-1}, and the fits corresponding to $\pm 1\sigma$ errors are shown in the blue lines with the intercepts of 5.76 and 6.13 km s^{-1}, respectively.

4.2 Investigating line broadening and the rotational velocity

To disentangle the line-broadening contributions, we selected 51 lines from the 67 lines used in Section 3 by adopting those with the least-blended (most symmetric) profiles. The profile fitting calculations yielded the results of v_T and then v_{rm}. An example of the typical fitting is shown for the Fe I 5569 Å line with its $W_\lambda = 44.4$ mÅ in Fig. 1. The converged solution of fitting gives $v_{rm} = 6.6$ km s^{-1} and an abundance of log Fe I = 6.73, which agrees well with the final abundance of log Fe = 6.79 (corresponding to [Fe/H] = −0.71), demonstrating that our fitting procedure works well.

The behaviour of v_{rm} derived from 51 lines is shown as a function of W_λ in Fig. 2. When we estimate the rotation velocity v_r from the projected rotation velocity $v_r \sin i$, we must separate the macroturbulence v_m from v_{rm}. The separation procedure requires a sophisticated approach such as the one adopted by Gray (2014), who analysed $v \sin i$ of five early-A slow rotators by deriving the radial-tangential macroturbulence (ζ_{RT}) from the Fourier transforms of the observed line profiles, based on spectra with very high S/N of 370–1840. His sample stars had $v \sin i = 6.0$–26.2 km s^{-1}, along with $\zeta_{RT} = 5.7$–2.0 km s^{-1}. For example, *o* Peg had $v \sin i = 6.0$ km s^{-1} and $\zeta_{RT} = 5.7$ km s^{-1}; α Dra had $v \sin i = 26.2$ km s^{-1} and $\zeta_{RT} = 2.0$ km s^{-1}. From these results, Gray suggested that even with

the relatively large uncertainties in ζ_{RT}, there may be a connection between ζ_{RT} and $v \sin i$, in that larger rotation may result in smaller macroturbulence. However, with the radial-tangential macroturbulence formulation having being set up with solar granulation in mind, Gray was cautious of its application to A stars without large convective envelopes. Taking into account his discussions (Gray 2014) and the lower quality (S/N = 100–120) of our spectrum, we did not attempt to separate v_m from v_{rm}. Since $v_{rm} < 8$ km s^{-1} (Fig. 2), ζ_{RT} may account for the majority of v_{rm}.

Following the suggestion described in Section 4.1 that v_{rm} is least influenced by local velocity fields in the weak-line limit as $W_\lambda \to 0$ mÅ, we adopted the intercept of the v_{rm} axis of the linear least-squares fit shown in Fig. 2, $v_{rm,0} = 5.9 \pm 0.2$ km s^{-1}, as the *apparent* projected rotation velocity, $v_a \sin i$. The error bar is the error in the value of the intercept taking into account errors in both coordinates.

It is found that $v_{rm,0} = 5.9$ km s^{-1} is consistent with v_{rm} shown in Table 2 for the lines of Cr II, Ti II and Fe I. We also calculated v_{rm} for 19 lines of Fe II, and found the intercept value of the least-squares fit to the plot of v_{rm} versus W_λ to be 7.0 ± 0.3 km s^{-1}, which is in acceptable agreement with $v_{rm,0} = 5.9 \pm 0.2$ km s^{-1}. Hence we are confident of the validity of choosing Fe I lines for the determination of the rotation velocity.

Our *apparent* projected rotation velocity $v_a \sin i = 5.9 \pm 0.2$ km s^{-1} confirms that our target is a very slow rotator, as Kurtz et al. (2014) found asteroseismically. The $v_r \sin i = 1$ km s^{-1} predicted by Kurtz et al. (2014) is well-supported. We therefore suggest that the difference between our measured $v_a \sin i$ and their prediction is significant for exploring macroturbulence and the pulsational velocity fields in the atmosphere of this star.

5 ABUNDANCE ANALYSIS

Abundances for the selected elements were determined using the SPTOOL software package based on the final model atmosphere. Its SPSHOW program was used to measure W_λ of lines of the elements by Gaussian profile fitting in most cases, but direct integration in others, and the program WIDTH was used to derive abundances from W_λ. Atomic data of wavelengths, χ, and log *gf* values are based on Kurucz & Bell (1995), but when updated log *gf* values were available from Castelli & Hubrig (2004), those were adopted instead. Table B1 in the Appendix shows the atomic data, W_λ, and the abundances derived from each line together with the average abundances for each ion and the number of lines used.

We searched for a magnetic field by applying the method of Mathys (1990), which uses the ratio of the strengths of the Fe II 6147.7 Å and 6149.2 Å lines to estimate the mean magnetic field modulus $\langle H \rangle$. Within the errors, we found no significant difference in strength between these two magnetically sensitive Fe II lines, hence our analysis proceeded with the assumption of no magnetic broadening. It should be noted, however, that within the errors we cannot rule out a magnetic field strength of the order of 1 kG.

We treated the Li doublet as a single line because only an upper limit for equivalent width could be measured, as noted in Table B1. The upper limit of W_λ was estimated to be 0.4 mÅ by the Cayrel (1988) formula for $\delta x = 0.014$ Å, $w = 6708$ Å$/R$ (at spectroscopic resolution $R = 160\,000$) and S/N=110.

The abundances of other doublet or triplet lines were obtained using the program MPFIT via Gaussian profile fitting (denoted as 'doublet fit' or 'triplet fit' in Table B1.) When hyperfine splitting (HfS) components and relative isotopic fractions of odd nuclei are both available and significant for a given line, the Gaussian profile fitting takes the HfS components and relative isotopic fractions

Table 3. Summary of abundances of each element. Average abundances of log X for element X are given in the thrid column. Standard deviations of each log X, uncertainties due to error bars of T_{eff}, $\log g$, and ξ (labelled t$g\xi$ in Column 7), and total uncertainties are given in the sixth, seventh and eighth columns, respectively. The numbers of doublet or triplet lines, and lines of hyperfine structure (HfS) fit used to derive the abundances, are given in the remarks column. The uncertain abundances are noted as 'uncertain' in the remarks. Solar abundances from Asplund et al. (2009) are listed in the last column.

Code	Ion	log X average	[X/H]	[X/Fe]	Std. dev. 1σ	Error t$g\xi$	Total error	No. of lines	Remark	Sun
3.00	Li I	≤1.38	≤0.33	≤1.04	...	...	...	1	One doublet	1.05
6.00	C I	7.82	−0.61	0.10	0.15	0.05	0.16	10	Two doublets	8.43
8.00	O I	8.38	−0.31	0.40	0.09	0.09	0.13	3	Three triplets	8.69
11.00	Na I	5.75	−0.49	0.22	0.04	0.04	0.06	4	One doublet	6.24
12.00	Mg I	7.13	−0.47	0.24	0.04	0.06	0.07	3		7.60
12.01	Mg II	7.29	−0.31	0.40	...	0.11	0.11	1	One triplet	7.60
14.00	Si I	7.05	−0.46	0.25	0.22	0.04	0.22	14		7.51
14.01	Si II	7.03	−0.48	0.23	0.07	0.08	0.11	3		7.51
16.00	S I	6.87	−0.25	0.46	0.08	0.03	0.09	8	One doublet, three triplets	7.12
20.00	Ca I	5.95	−0.39	0.32	0.12	0.07	0.14	25		6.34
20.01	Ca II	6.02	−0.32	0.39	0.09	0.06	0.11	3		6.34
21.01	Sc II	2.80	−0.35	0.36	0.15	0.06	0.16	9	Four HfS fit	3.15
22.00	Ti I	4.59	−0.36	0.35	0.11	0.06	0.13	15		4.95
22.01	Ti II	4.59	−0.36	0.35	0.18	0.06	0.19	32		4.95
24.00	Cr I	4.90	−0.74	−0.03	0.11	0.07	0.13	14		5.64
24.01	Cr II	4.96	−0.68	0.03	0.12	0.05	0.13	21		5.64
25.00	Mn I	4.57	−0.86	−0.15	0.05	0.06	0.08	7	Two HfS fit	5.43
26.00	Fe I	6.79	−0.71	0.00	0.10	0.08	0.13	67		7.50
26.01	Fe II	6.79	−0.71	0.00	0.14	0.08	0.16	21		7.50
28.00	Ni I	5.70	−0.52	0.19	0.10	0.06	0.12	41		6.22
29.00	Cu I	3.56	−0.63	0.08	0.05	0.07	0.09	2	Uncertain	4.19
30.00	Zn I	4.15	−0.41	0.30	0.03	0.06	0.07	3		4.56
39.01	Y II	1.87	−0.34	0.37	0.06	0.07	0.09	7		2.21
40.01	Zr II	2.38	−0.20	0.51	...	0.06	0.06	1	Uncertain	2.58
56.01	Ba II	1.58	−0.60	0.11	0.04	0.15	0.15	4	Four HfS fit	2.18
58.01	Ce II	1.26	−0.32	0.39	...	0.08	0.08	1	Uncertain	1.58
60.01	Nd II	0.91	−0.51	0.21	...	0.09	0.09	1	Uncertain	1.41

into account. Test calculations demonstrated that lines with relative isotopic fractions less than 0.1, or with $W_\lambda \leq 20$ mÅ, yield negligible differences that are less than 0.02 dex between abundances with and without HfS components and isotopic fractions. We adopted HfS components and isotopic fractions from Kurucz (2011)[4] for Sc II and Mn I, and from McWilliam (1998) for Ba II. The corresponding lines are labelled as 'HfS fit' in Table B1. The resulting abundances of each element are summarized in Table 3.

To illustrate the abundance pattern relative to the Sun, we depicted [X/H] against atomic number in the top panel of Fig. 3. All elements show clear underabundances in the range −0.2 to −0.9 dex, except for Li, which is derived with an upper limit, only. The systematic underabundances are consistent with the remarkably deficient Fe abundance, [Fe/H] = −0.71 dex, most unusual among main-sequence A stars with very slow rotation, almost all of which are Am or Ap stars. Thus, the observed pattern is *not* characteristic of Am or Ap stars, where Fe-peak and rare-earth elements are overabundant (e.g. Smith 1971; Adelman 1973) – often dramatically so.

The abundances of volatile elements, namely C and O, are also important for distinguishing metal-poor stars from the chemically peculiar class of λ Boo stars, which have Fe-peak elements that are underabundant, but volatile elements that are solar (Stürenburg 1993). Since we observe the volatile elements to be sub-solar in KIC 11145123, we conclude it is not a λ Boo star, either.

[4] http://kurucz.harvard.edu/linelists/gfhyperall/
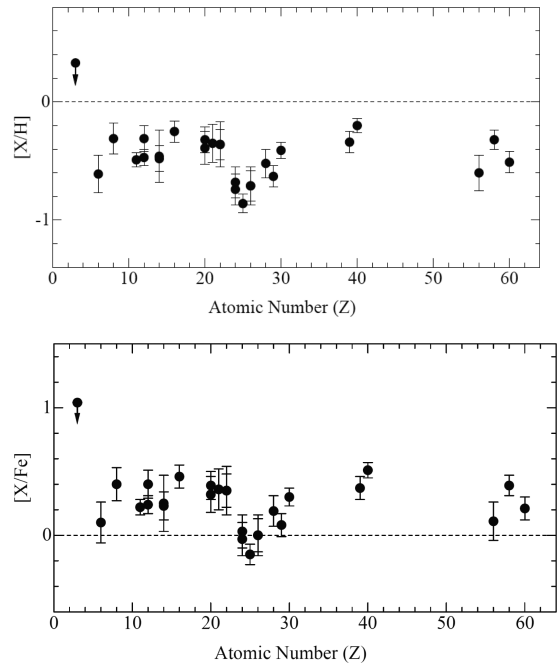
Figure 3. Top panel: [X/H] against atomic number for KIC 11145123. Except for Li, which is derived as an upper limit only, the systematic underabundances are consistent with the remarkably deficient Fe abundance, [Fe/H] = −0.71 dex. Bottom panel: [X/Fe] against atomic number for KIC 11145123.

The abundance pattern relative to Fe is shown in the bottom panel of Fig. 3, where enhancements of [X/Fe] $\sim$ 0.1–0.5 dex can be seen for all elements except Mn and Cr. The behaviour of [X/Fe] for α elements (C, O, Mg, Si, S, Ca and Ti) resembles those well known among metal-poor stars. Y, Zr, Ba and rare-earth elements show similar enhancements of $\sim$0.1–0.5 dex. As established in the pattern of [X/H], the pattern of [X/Fe] again is inconsistent with characteristics of Am and Ap stars. We discuss this further in Sections 7.4.1 and 7.4.2.

6 MODEL

It is a well-known problem that model frequencies in δ Sct and γ Dor stars are difficult to match to the precision of the observed frequencies. Nevertheless, to proceed it is assumed that finding a 'best model' – one that has frequencies close to the observed ones – is an informative procedure that gives some real information on the evolutionary state and structure of the star. In their discovery paper of the core-to-surface rotation of KIC 11145123, Kurtz et al. (2014) tried to find asteroseismic stellar models that best fitted the pulsation frequencies – particularly the g-mode series of frequencies and some of the p-mode frequencies.

So Kurtz et al. (2014) suggested that the star is near the TAMS, has enhanced helium abundance and perhaps has low metallicity. This led to the conjecture that KIC 11145123 is a Population II star, which was the impetus for our acquiring the high-resolution Subaru spectrum and carrying out this study. As we have seen in Section 5, KIC 11145123 has very low metallicity, hence we have searched for models consistent with observed pulsation frequencies of KIC 11145123 in the same way as described in Kurtz et al. (2014), except that we have adopted here much lower metallicity, $Z = 0.003$, according to the spectroscopic analysis in this paper.

Kurtz et al. (2014) obtained rotationally split high-order dipole g-mode as well as p-mode frequencies from the *Kepler* photometric data. To constrain our models we used the mean period separation of the dipole g modes, ΔP_g (rather than each g-mode frequency) and the frequencies of the five largest-amplitude p modes; for rotational multiplets, the central frequencies (corresponding to zonal modes) were used.

It is difficult to determine precisely the period spacing of the g modes of KIC 11145123 because this slightly depends on the range of periods and it has some irregularities (see fig. 6 in Kurtz et al. 2014). We adopted $\Delta P_g = 0.0245 \pm 0.0002$ d for the purpose of constraining our models, although the models obtained are not very sensitive to the exact value of ΔP_g.

The largest-amplitude p mode at a frequency of 17.964 d^{-1} (ν_1; we follow the frequency nomenclature of Kurtz et al. 2014, where this is ν_1, and so on for further frequencies below) shows no rotational splitting – it is a singlet; this is considered to be a radial mode. The other four large amplitude frequencies, 18.366 d^{-1} (ν_2), 16.742 d^{-1} (ν_3), 19.006 d^{-1} (ν_4) and 22.002 d^{-1} (ν_5), are triplets and quintuplets; i.e. non-radial modes of $\ell = 1$ and 2. We first obtained models having ΔP_g and a radial mode consistent with ν_1, then we examined the consistency with the other four p modes by calculating the mean deviation of the frequencies, and by comparing T_{eff} and log g with the spectroscopic values of KIC 11145123 derived in Section 3 and also given in Table 1.

Evolutionary models were calculated using Modules for Experiments in Stellar Evolution (MESA; Paxton et al. 2013) with the same settings as in Kurtz et al (2014): i.e. the heavy element abundance, $Z = 0.003$, was scaled by the solar mixture of Asplund et al. (2009); the radiative OPAL opacity tables (Iglesias & Rogers
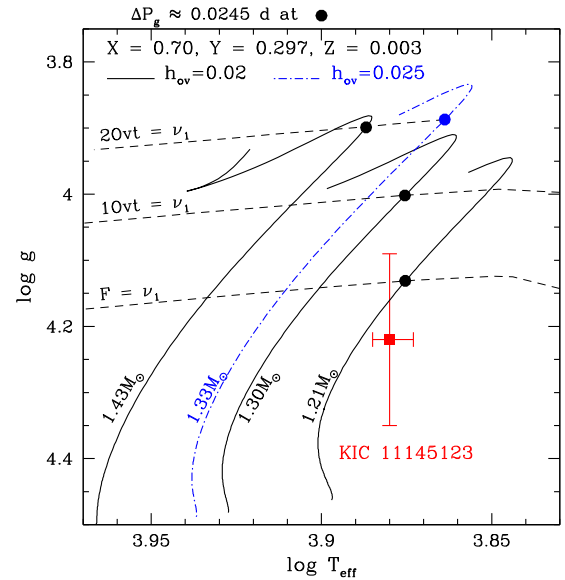

Figure 4. Logarithmic effective temperature, log T_{eff}, versus surface gravity, log g, diagram. Some main-sequence evolutionary tracks for a chemical composition of $(X, Z) = (0.7, 0.003)$ are shown by solid and dash–dotted lines. The solid lines correspond to models with a core-overshooting parameter of $h_{ov} = 0.02 \approx \alpha_{ov}/10$, while the dash–dotted line corresponds to $h_{ov} = 0.025$. Each horizontal dashed line indicates the locus where the largest-amplitude pulsation frequency of KIC 11145123 ($\nu_1 = 17.964$ d^{-1}) is equal to the radial fundamental (F) mode, the first overtone (1Ovt) mode or the second overtone (2Ovt) mode frequency. A big dot on an evolutionary track indicates the position where the mean period spacing of high-order dipole g modes is $\Delta P_g = 0.0245$ d (the observed value); ΔP_g decreases with evolution (see e.g. Kurtz et al. 2014). A horizontal dashed line does not necessarily cross a track at a dot, although such tracks are selected in this diagram. The position of KIC 11145123 with error bars is based on the spectroscopic results summarized in Table 1.

1996) were used; and mixing length was set equal to 1.7 H_p, where H_p is the pressure scale height. Atomic diffusion was activated in the code to erase noise in the Brunt–Väisälä frequency. The parameters specifying an evolutionary track are mass, initial chemical composition (X, Z), and a core-overshooting parameter h_{ov}, in which $h_{ov}H_p$ gives an exponential decay length of mixing efficiency (Herwig 2000) above the convective core boundary. (Another often used overshooting parameter α_{ov}, in which a step-wise mixing in a range of $\alpha_{ov}H_p$ is assumed, approximately corresponds to $10h_{ov}$.)

As evolution of the stellar model proceeds for a given set of parameters, the mean period spacing ΔP_g decreases gradually, and at a particular evolutionary stage it becomes equal to the observed value 0.0245 d, shown as a big dot in Fig. 4 for four different evolutionary tracks. However, for most models no radial mode of the model reproduces ν_1. When that was the case we changed the mass slightly and repeated the calculation until we obtained a model that reproduced both ΔP_g and ν_1. This corresponds, in Fig. 4, to the positions of the filled circles, where the evolutionary tracks cross a horizontal dashed line.

Since it is possible for ν_1 to be identified as either the fundamental (F) mode, the first overtone (1Ovt) mode, or the second overtone (2Ovt) mode, we find, in general, three such models for a given set of (X, Z, h_{ov}). Fig. 4 shows the locations in the log T_{eff} − log g plane of three models with $(X, Z, h_{ov}) = (0.70, 0.003, 0.02)$ and one model with $(0.70, 0.003, 0.025)$. For a given X, larger h_{ov} yields a cooler
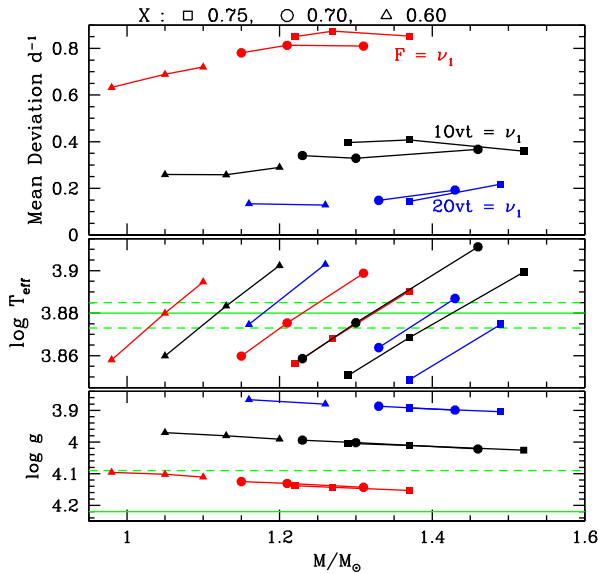
Figure 5. The surface gravity (bottom panel), the effective temperature (middle panel) and the mean deviation from observed p-mode frequencies (top panel) of each model satisfying the conditions of $\Delta P_g \approx 0.0245$ d and a radial mode frequency equal to ν_1 (i.e. dots crossing one of the horizontal dashed lines in Fig. 4) are plotted. Different symbols are used for models with different initial hydrogen abundances ($X = 0.75, 0.70, 0.60$). For a given X, some values for the overshooting parameter h_{ov} in a range between 0.01 and 0.03 are adopted to obtain models with T_{eff} close to the spectroscopic value of KIC 11145123. Models with the same X but different h_{ov} are connected by lines. Red, black and blue colours are used for models which identify the observed ν_1 as the fundamental (F) mode, the first overtone (1Ovt) mode or the second overtone (2Ovt) mode, respectively (see top panel). The spectroscopic values of $\log T_{eff}$ and $\log g$ and their error ranges of KIC 11145123 are shown by horizontal lines.

model, so that we can tune h_{ov} to have a model with T_{eff} consistent with the spectroscopic value of KIC 11145123.

Mean deviations of $\nu_2 \ldots \nu_5$ of KIC 11145123 from the models thus obtained are shown in Fig. 5, in which T_{eff} and $\log g$ are also compared with those of KIC 11145123. The mean deviations for the models with ν_1 being identified as second radial overtone modes (2Ovt) are in most cases less than 0.2 d^{-1} (i.e. less than ~ 1 per cent); these are significantly smaller than those of the models with ν_1 being identified as the fundamental radial overtone (F). However, the surface gravities of the models that identify ν_1 as belonging to the second radial overtone (2Ovt) are lower than the spectroscopically measured $\log g = 4.22 \pm 0.13$ (Table 1) by about 2.4σ. On the other hand, although models that identify ν_1 with the fundamental radial mode (F) have surface gravities more consistent with the spectroscopic value, the mean deviations of the pulsation frequencies are much higher (~ 5 per cent). It is not clear at present how to tune the models for better consistency with the observations. It seems probable that the internal structure of KIC 11145123 deviates considerably from the structure of the models calculated assuming single-star evolution; further fine-tuning of the models needs a dedicated study of the internal structure of non-standard models.

We note that models with a larger initial hydrogen abundance are slightly more massive, but the mean deviations hardly depend on X. A hydrogen abundance of $X = 0.75$ (corresponding to $Y = 0.247$) is probably close to normal for a $Z = 0.003$ single star. However, the ages of the $X = 0.75$ models are ~ 1.5–3×10^9 yr, which

are too young for a single star, having evolved normally in our Galaxy, to have the low metallicity of $Z = 0.003$ ([Fe/H] = -0.7) of KIC 11145123.

7 DISCUSSION

To clarify the properties of our target, we discuss the atmospheric parameters, the rotation velocity and the abundance pattern in this section. We discuss interpretations of these and the asteroseismic results in terms of a blue straggler.

7.1 Atmospheric parameters

We determined the atmospheric parameters of T_{eff}, $\log g$, ξ and [Fe/H] spectroscopically, using Fe I and Fe II lines. Values of T_{eff}, $\log g$ and [Fe/H] are also available from broad-band photometry and colour indices from the automated analysis of Huber et al. (2014). There are differences between our values and those of Huber et al. (2014), which are $\Delta T_{eff} = -461$ K, $\Delta \log g = +0.25$ and Δ[Fe/H] = -0.57 dex, in the sense [(ours) $-$ (Huber et al.)].

While we fully expect that our atmospheric parameters from our high-resolution, high S/N spectra are more accurate than those from much lower resolution broad-band photometry, to examine the validity of our derived parameters further, we compare them with those of 117 *Kepler* A and F stars investigated by Niemczura et al. (2015), who obtained the final values of these parameters using Fe I and Fe II lines based on high-resolution spectra, in the same manner as we did. They compared the behaviour of the parameters between their values and those of Huber et al. (2014), taking differences of each parameter into account.

For T_{eff}, fig. 3(a) of Niemczura et al. (2015) depicts the behaviour of $\Delta T_{eff} = T_{eff}$ (SPEC) $-$ T_{eff} (H2014) [where T_{eff} (SPEC) is their value and T_{eff} (H2014) that of Huber et al. (2014)], which has large scatter of ± 600 K as a function of T_{eff} (SPEC). When we plot our $\Delta T_{eff} = -461$ K in their fig. 3(a), it is included in the negative scatter range. Niemczura et al. (2015) suggested that the accuracy of their spectroscopic temperatures is supported because the temperatures derived from spectral energy distributions agree well with T_{eff} (SPEC) within a scatter of about ± 300 K. According to their suggestion, and from an evaluation of the quality of each method, we consider our atmospheric parameters, T_{eff}, $\log g$ and [Fe/H], to be more reliable than those from broad-band photometry. This is unsurprising.

The values of microturbulence ξ derived by Niemczura et al. (2015) are plotted in their fig. 5. Our ξ is consistent with the behaviour of non-chemically peculiar stars at $T_{eff} \sim 7600$ K.

7.2 Rotation velocity and magnetic braking; Ap stars

Our apparent projected rotation velocity, $v_a \sin i = 5.9 \pm 0.2$ km s^{-1}, is extremely slow compared with the distribution of $v \sin i$ for the stars with similar temperatures in the range $7000 \leq T_{eff} \leq 8000$ K (Niemczura et al. 2015). Their fig. 7(e) shows, and their electronic table 3 lists, values of $v \sin i$ distributed between 8 and 260 km s^{-1}, but mostly between 50 and 150 km s^{-1} (note that they do not take into account macroturbulence, hence their minimum $v \sin i$ is overestimated.). Thus, the reason why KIC 11145123 rotates so slowly is unclear; this important point needs to be explored: Why does KIC 11145123 rotate so slowly compared with the majority of A and early F stars?

It is well known that Ap stars with magnetic fields rotate more slowly than normal A stars. Stępień (2000) suggested that magnetic
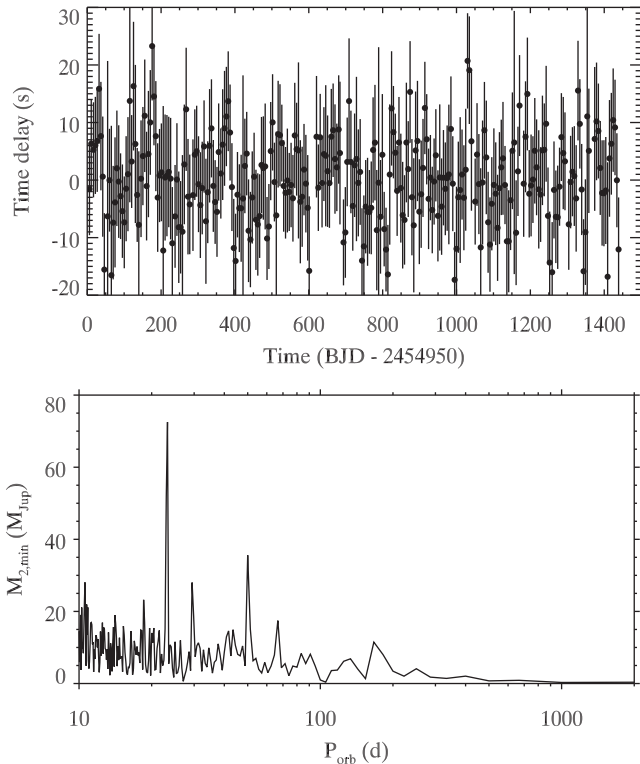
Figure 6. Top: time delays derived from the p-mode singlet. Bottom: upper limits on $M_{2,\mathrm{min}}$ from the Fourier analysis of the time delays.

Ap stars become slow rotators due to loss of angular momentum by magnetic braking in the pre-main-sequence phase. While our search for a magnetic field in KIC 11145123 yielded a null result, it did not rule out a field strength of the order of 1 kG, which is typical of the field strengths found in many Ap stars. However, our abundance analysis clearly shows that KIC 11145123 is not an Ap star – as we argue in Section 7.4.2 – hence we take the null result for the magnetic measurement to be correct, and conclude that magnetic braking is not a viable hypothesis for the remarkably slow rotation of this star.

7.3 Phase modulation and a stringent upper limit on the mass of any companion; Am stars

It is well known that metallic-lined A stars – the Am stars – are relatively slow rotators with $v \sin i \leq 100\ \mathrm{km\ s}^{-1}$ (Abt 1967). These stars are typically in close binary systems with orbital periods of 1–10 d, where spin–orbit synchronization has slowed the rotation of the Am star. This slow rotation is a requisite for the effects of atomic diffusion to alter the atmospheric abundances in Am stars. We therefore searched for evidence of a binary companion to KIC 11145123.

We found no evidence of such a companion, and have derived stringent upper limits for the allowable mass of any possible companion using the phase modulation (PM) method (Murphy et al. 2014; Murphy & Shibahashi 2015). We divided the data into 5-d segments to search for changes in the pulsation phase that could be caused by binary motion. Phase changes were converted into time delays, which are shown in the top panel of Fig. 6. We used only the p-mode singlet; the g modes and non-radial p modes are rotationally split, and the azimuthal components are not resolved in 5-d light-curve segments. To improve the precision we pre-whitened all other

peaks in the Fourier transform of the light curve with amplitudes exceeding 0.2 mmag. The lower panel of Fig. 6 shows the upper limits to $M_{2,\mathrm{min}}$ in the 10–2000 d period range. A companion with $M_{2,\mathrm{min}}$ consistent with a brown dwarf could exist at some periods, but the peaks in the lower panel of Fig. 6 could be caused by residual low-amplitude oscillations near the p-mode singlet instead.

We thus find that no stellar mass companion is present for orbital periods of 10–2000 d from our PM analysis, and shorter periods of 1–10 d would produce ellipsoidal variation in the high-precision Kepler light curve. We certainly rule out rotation and orbital coupling in a 100-d binary. The caveat is that this is dependent on the orbital inclination; if there were a companion in an orbit with very low inclination, then we would be insensitive to that, both in the PM analysis and in the ellipsoidal variations. However, Kurtz et al. (2014) showed that the g-mode pulsations have very low visibility of the axisymmetric modes, which strongly suggests that the modes have high inclination. Unless there is a strong misalignment of the purported orbital inclination and the pulsation axis, this also argues against any companion. Finally, no F, G or K main-sequence companion can be present because we would see evidence in our high-resolution spectra.

With our abundances – discussed in detail in the next section – and these arguments, we conclude that KIC 11145123 is not an Am star and that it is *currently* not in a binary system. Thus, orbital synchronization is not the cause of the slow rotation. However, we return to this latter conclusion in the discussion below – and this is the reason we italicized '*currently*' – because we conjecture that previously KIC 11145123 may have been in a binary system to give it its current blue straggler stellar structure.

7.4 Abundance pattern

In this section we compare the abundance patterns relative to Fe in our target and in Am, Ap and blue stragglers to clarify the properties of our target and to give an answer to the prediction by Kurtz et al. (2014) that our target is either an Am star or a blue straggler.

7.4.1 Comparison with Am stars

In the top panel of Fig. 7 we compare the abundance pattern (except for Li) of KIC 11145123 with those of the average abundances of the 96 normal A–F stars and 13 Am stars adopted from Niemczura et al. (2015).

The abundance pattern of our target is consistent with that of normal A–F stars, and inconsistent with that of Am stars because the typical underabundances of Ca and Sc, and overabundances of Ba and rare-earth elements, for Am stars are not observed. Hence we conclude that our target is not an Am star.

7.4.2 Comparison with roAp stars

In the bottom panel of Fig. 7 we compare the abundance pattern of our target with those of the same normal A–F stars as adopted above, and the average abundance pattern of five roAp stars: HD 203932, Gelbmann et al. (1997); 10 Aql, β CrB, and 33 Lib, Ryabchikova et al. (2004); KIC 4768731, Niemczura et al. (2015); and one δ Sct star with an Ap chemical signature: HD 41641, Escorza et al. (2016).

The abundance pattern of our target is not consistent with those of roAp stars: C and O are not underabundant, and rare-earth elements show no enhancement. The abundance pattern is consistent with that
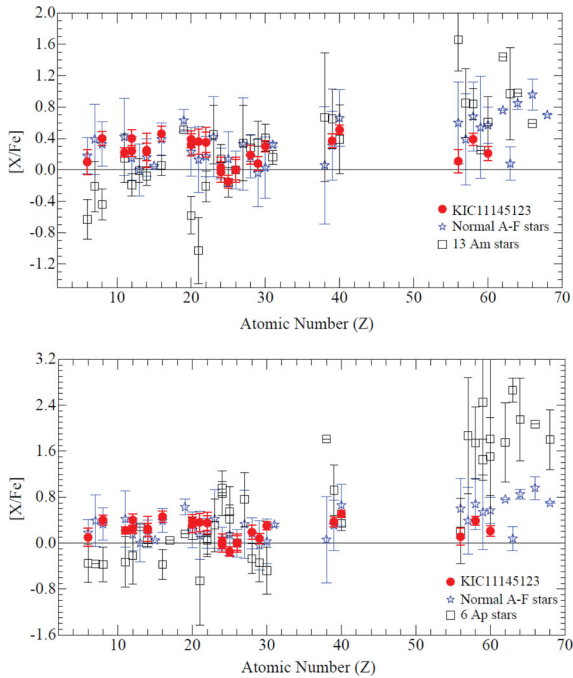
Figure 7. Top panel: comparison of abundance patterns between our target and normal A/F and Am stars. Bottom panel: comparison of abundance patterns between our target and normal A/F stars, and the average abundance pattern of five roAp stars and one δ Sct star with an Ap chemical signature. From these comparisons we conclude that KIC 11145123 is neither an Am star nor an Ap star.
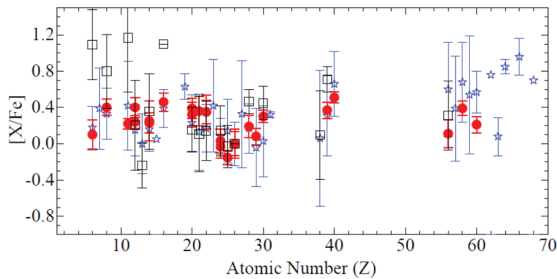
Figure 8. Comparison of abundance patterns between our target (filled circles) and normal A/F stars (stars) and 25 λ Bootis stars (open squares). The systematic enhancement of volatile elements of C, O, Na and S that is observed in λ Boo stars is not seen in our target star. KIC 11145123 is not a λ Boo star.

of normal A–F stars, just as in the comparison with Am stars. Hence we conclude that our target is not an Ap star, rapidly oscillating or otherwise.

7.4.3 Comparison with λ Boo stars

Fig. 8 compares the abundance patterns of KIC 11145123, normal A/F stars and 25 λ Bootis stars. The sample of λ Boo stars consists of nine, six and 10 stars adopted from Stürenburg (1993), Paunzen et al. (1999) and Heiter (2002), respectively, which are confirmed as λ Boo stars by Murphy et al. (2015), and their average abundances are plotted in Fig. 8. The volatile elements C, O, Na and S show enhancement of ∼1 dex compared to Fe, in contrast to KIC 11145123 and also to normal A/F stars. We therefore conclude that KIC 11145123 is not a λ Boo star.
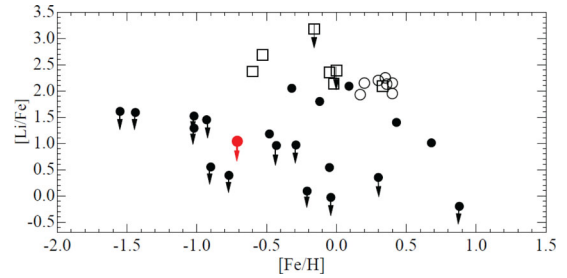
Figure 9. Behaviour of [Li/Fe] versus [Fe/H] for our target (a red filled circle), 20 high-velocity A–F stars (Glaspey et al. 1994, black filled circles), and normal A stars (Takeda et al. 2012, open squares; Burkhart & Coupry 2000, open circles).

7.4.4 Comparison with blue stragglers

KIC 11145123 has a large radial velocity of $V_h = -135.4 \pm 0.2$ km s^{-1}. We do not have a parallax, therefore no distance measurement, but can get a rough estimate of distance from the luminosity of the best asteroseismic models of Kurtz et al. (2014), who give $\log L/L_\odot = 1.1$, and the approximation that the *Kepler* magnitude, Kp = 13.1, is close to Johnson *V*. Together those give a distance of about 1.7 kpc. The galactic longitude of KIC 11145123 is 81°.7, which means the star is nearly in the direction of galactic rotation. With the approximate distance, it is easy to calculate that KIC 11145123 is at about the same distance from the galactic centre as is the Sun. If we assume that the observed radial velocity of KIC 11145123 is close to the component of its peculiar velocity along the direction of Galactic rotation, given the Sun's galactic orbital velocity of 220 km s^{-1} and its component of the peculiar velocity $V_\odot = 5.2$ km s^{-1}, the large velocity of approach of KIC 11145123 of −135 km s^{-1} shows it, therefore, to be orbiting in the direction of rotation of the Galaxy with the rotation component of $\Theta = 90$ km s^{-1} – albeit much more slowly than the Sun and typical Population I stars – indicating that it is a halo, or runaway star. The galactic latitude of KIC 11145123 is 12°.5, which at a nominal distance of 2 kpc puts it about 400 pc above the galactic plane, near the edge of the thin disc, of which it is probably not a member. Without a parallax and proper motion, we cannot characterize the space motions more than this at present, but these properties, along with the low metallicity, are shared with the blue stragglers that are known to exist in many globular clusters, old open clusters, and among the field Population II stars in the Galactic bulge and halo (e.g. Glaspey et al. 1994; Lovisi et al. 2013a).

As a final discussion on the abundance pattern of our target, we compare our target with blue stragglers in the abundances of Li, C and O. In Fig. 9 we depict the behaviour of [Li/Fe] as a function of [Fe/H] for the 20 high-velocity A–F stars taken from Glaspey et al. (1994, table 3) and our target. They identified the 15 Li-weak stars as halo and thick-disc blue stragglers, or old and mostly thin-disc blue stragglers, of which 13 stars are shown with upper limits on the Li abundance. We also plot [Li/Fe] of 14 normal A stars taken from Takeda et al. (2012) and Burkhart & Coupry (2000).

As can be seen from Fig. 9, the [Li/Fe] of our target is certainly lower than those of normal A stars and a few Li strong stars of Glaspey et al. (1994), but is compatible with the Li-weak blue stragglers. The low abundance of Li on its own argues that KIC 11145123 during its lifetime has had a thick surface convection zone that took ^{7}Li down to levels where the temperature was 2.4 MK, where it is destroyed in fusion reactions. Main-sequence A and early F stars do not have convection zones thick enough to do
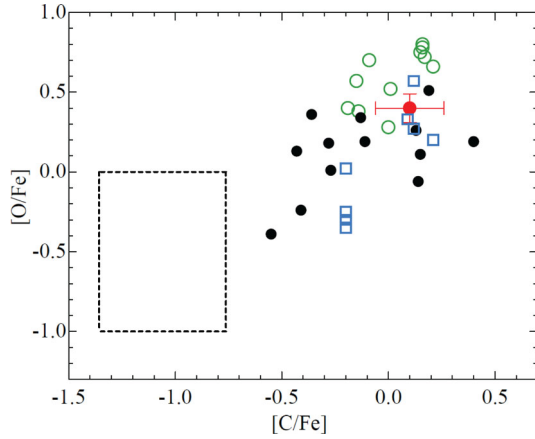
Figure 10. Behaviour of [O/Fe] versus [C/Fe] for the blue stragglers in the globular clusters NGC 6752 (Lovisi et al. 2013a, black filled circle) and M 4 (Lovisi et al. 2010, green open circle), and for turn-off dwarf stars in NGC 6752 (Carretta et al. 2005, blue open square). Our target is shown with a red filled circle. The distribution of CO-depleted blue stragglers (Ferraro et al. 2006) is shown as the box with a dashed line.

this. We therefore deduce that KIC 11145123 had an earlier main-sequence, or post-main-sequence, life with a convection zone thick enough to reach the temperature of Li burning.

In Fig. 10 we illustrate the behaviour of [O/Fe] versus [C/Fe] for our target and the blue stragglers in the globular clusters of NGC 6752 and M 4 adopted from Lovisi et al. (2013a) and Lovisi et al. (2010), respectively. The turn-off dwarf stars in NGC 6752 adopted from Carretta et al. (2005) and the distribution region of the CO-depleted blue stragglers in 47 Tuc adopted from Ferraro et al. (2006) are shown for comparison.

The adopted sample of blue stragglers in NGC 6752 has $\log g \sim 4$ and $v \sin i < 40 \, \mathrm{km \, s^{-1}}$ – consistent with those of our target – while [Fe/H] (~ -1.5 dex) is different. The sample of blue stragglers in M4 shows $v \sin i < 5 \, \mathrm{km \, s^{-1}}$ in most cases, but is different in [Fe/H] (~ -1.3 dex) and radial velocities ($+70$ to $+90 \, \mathrm{km \, s^{-1}}$). The turn-off dwarf stars in NGC 6752 overlap with these blue stragglers. These blue stragglers and turn-off dwarf stars are clearly distributed in a different region outside the region of CO-depleted blue stragglers in 47 Tuc. Our target's location is compatible with the observed abundances of both the blue stragglers and the turn-off dwarf stars. Lovisi et al. (2010, 2013a) found that there is no depletion of C and O abundances in their samples of blue stragglers with slow rotation, and suggested that the studied blue stragglers in M4 and NGC 6752 may derive from stellar collisions, for which no chemical anomalies are expected.

Taking into account the consistencies found in the behaviour of Li, C, and O between our target and the blue stragglers, we conclude that our target is a blue straggler.

7.5 Summary of the spectroscopic analysis

We analysed the properties of our target, KIC 11145123, based on high-dispersion spectra obtained by HDS on the Subaru telescope. We summarize the results of the spectroscopic analysis of our target as follows.

(1) The atmospheric parameters are derived from the Fe I and Fe II lines: $T_{\mathrm{eff}} = 7590^{+80}_{-140}$ K, $\log g = 4.22 \pm 0.13$, $\xi = 3.1 \pm 0.5 \, \mathrm{km \, s^{-1}}$ and [Fe/H] $= -0.71 \pm 0.11$. The T_{eff} and [Fe/H] values are more reliable than the values derived from photometric colours

given in the KIC. The low [Fe/H] value is unusual among late-A stars, implying that our target is a Population II star.

(2) The apparent projected rotation velocity $v_{\mathrm{a}} \sin i = 5.9 \pm 0.2 \, \mathrm{km \, s^{-1}}$ is consistent with the asteroseismically predicted $v_{\mathrm{eq}} = 1 \, \mathrm{km \, s^{-1}}$ convolved with macroturbulent and pulsational broadening.

(3) The comparisons of abundance patterns of [X/Fe] among our target, normal A–F stars, Am stars and roAp stars show that our target is neither an Am star nor an Ap star, but follows consistently the pattern of normal A–F stars.

(4) Our analysis of [Li/Fe], [C/Fe] and [O/Fe] abundances is consistent with our target being a blue straggler. This suggestion is consistent with the low [Fe/H], the slow rotation, and the high radial velocity of our target, which are well known to be observed in Population II stars.

8 CONCLUSION: THE BLUE STRAGGLER HYPOTHESIS

KIC 11145123 presents a problem. It is an exceedingly slowly rotating A star with a rotation period of 100 d, and is neither an Am or Ap star, and so cannot have lost angular momentum as those stars do. How did this star come to be so slowly rotating? This problem is not an isolated one for KIC 11145123. Other *Kepler* A stars that have had interior and surface rotation measured by asteroseismology also show unusually slow rotation (Saio et al. 2015; Murphy et al. 2016; Schmid & Aerts 2016). It is true that there is a selection effect in these first studies of core-to-surface rotation in that the rotational splitting in the non-radial mode multiplets is easier to see for slow rotation. Nevertheless, the slow rotation is real, and needs explanation.

We have found in this paper that KIC 11145123 has the attributes of a field blue straggler. It has low metallicity of [Fe/H] $= -0.71$. This alone probably requires that star to be older than the Sun, since it had to be born at a time and place in galactic history when the metallicity of the interstellar medium was less than that when and where the Sun was born. Since this is variable with position within the Milky Way, no precise age can be ascribed to KIC 11145123, but it certainly is much older than the ~ 1 Gyr lifetime of a main-sequence A star, hence it cannot have been born an A star. This is supported by our asteroseismic mass of 1.4 $\mathrm{M_{\odot}}$ for our best model of the star; this is much lower than the 1.7 $\mathrm{M_{\odot}}$ expected for a Population I A star of the same $T_{\mathrm{eff}} = 7600$ K and $\log g = 4.2$. And the radial velocity of $-135 \, \mathrm{km \, s^{-1}}$ shows the star to be Population II.

There is a time and age problem. If KIC 11145123 was born 5–10 Gyr ago, which would be consistent with its [Fe/H] $= -0.71$, then what has it been doing all this time to now be an A star with only a 1-Gyr main-sequence lifetime? We suggest that only merger or mass transfer in a binary system can account for this, and those are common pathways for stars to become blue stragglers. Yet both pathways present problems.

If we imagine a stellar merger, then KIC 11145123 would have started life as a much lower mass star. It would have been below the Kraft Break, hence would have had relatively slow rotation to begin with. The merger would have increased its mass to the current 1.4 $\mathrm{M_{\odot}}$ of our best asteroseismic model, mixed the interior and moved the star to the main-sequence with a somewhat enhanced He abundance, as in our best model. Mergers have been modelled with the formation of a circumstellar disc coupled to an ~ 200 G magnetic field to explain slow rotation of blue stragglers (Sills, Adams & Davies 2005), but those models do not specifically address the excessively slow rotation with a period of 100 d. As we have pointed

out, KIC 11145123 is far from the only A–F star in the *Kepler* data that shows excessively slow rotation. A common mechanism is needed to understand the rotation, hence for the merger model to apply in this case, it must be a common pathway to the formation of blue stragglers, rather than a rare one.

The other pathway to a blue straggler is for mass to be stripped by a companion in the evolution of a binary system. This, too, could leave the donor star with enhanced He abundance, and the change in structure with the mass loss could result in some internal mixing to get the resultant star back on to the main sequence with its new mass and structure. Mass loss could also shed angular momentum. This seems a more promising idea than merger. But, we have put stringent upper limits that the mass of any current companion must be less than stellar, if we accept that the amplitudes of the g-mode dipole triplets give some information on the rotation axis, and that there is not an extreme – say nearly $90°$ – spin–orbit misalignment in the purported binary. That leaves some room to manoeuvre in this scenario, but it, too, seems improbable, and we are looking for a mechanism that can produce many late-A and early-F very slowly rotating stars.

We do not have a suggestion that is consistent with all that we have learned of this star from our spectroscopic and asteroseismic studies. The star is Population II. It is metal poor and has high space velocity. It is not an Am or Ap star. It is on the main-sequence. It does have a 100-d rotation period. What is it and how did it get that way? We do not yet know. *Gaia* will provide a parallax and proper motion that will give better understanding of the star's space motion, but that is unlikely to give a definitive understanding of the evolutionary pathway to such an unusual object. Further information is more likely to come with the analysis of similar very slowly rotating A stars from existing *Kepler* data, and from data from the upcoming TESS mission.

ACKNOWLEDGEMENTS

REFERENCES

Abt H. A., 1967, in Cameron R. C., ed., Magnetic and Related Stars, Mono Book Co., Baltimore, p 173
Adelman S. J., 1973, ApJ, 183, 95
Asplund M., Grevesse N., Sauval A. J., Scott P., 2009, ARA&A, 47, 481
Burkhart C., Coupry M. F., 2000, A&A, 354, 216
Carretta E., Gratton R. G., Lucatello S., Bragaglia A., Bonifacio P., 2005, A&A, 433, 597
Castelli F., Hubrig S., 2004, A&A, 425, 263
Cayrel R., 1988, in Cayrel de Strobel G., Spite M., eds, Proc. IAU Symp. Vol. 132, The Impact of Very High S/N Spectroscopy on Stellar Physics. Kluwer Academic Publishers, Dordrecht, p. 345
Escorza A. et al., 2016, A&A, 588, A71
Ferraro F. R. et al., 2006, ApJ, 647, L53
Gelbmann M., Kupka F., Weiss W. W., Mathys G., 1997, A&A, 319, 630
Gizon L. et al., 2016, Sci. Adv., 2, e1601777
Glaspey J. W., Pritchet C. J., Stetson P. B., 1994, AJ, 108, 271
Gray D. F., 2014, AJ, 147, 81
Heiter U., 2002, A&A, 381, 959
Herwig F., 2000, A&A, 360, 952
Huber D. et al., 2014, ApJS, 211, 2
Iglesias C. A., Rogers F. J., 1996, ApJ, 464, 943
Kurtz D. W., Saio H., Takata M., Shibahashi H., Murphy S. J., Sekii T., 2014, MNRAS, 444, 102
Kurucz R., 1993, ATLAS9 Stellar Atmosphere Programs and 2 km/s grid. Kurucz CD-ROM No. 13. Smithsonian Astrophysical Observatory, Cambridge, Mass. p. 13
Kurucz R. L., 2011, Can. J. Phys., 89, 417
Kurucz R., Bell B., 1995, Atomic Line Data (R.L. Kurucz and B. Bell) Kurucz CD-ROM No. 23. Smithsonian Astrophysical Observatory, Cambridge, Mass. p. 23
Landstreet J. D., Kupka F., Ford H. A., Officer T., Sigut T. A. A., Silaj J., Strasser S., Townshend A., 2009, A&A, 503, 973
Lovisi L. et al., 2010, ApJ, 719, L121
Lovisi L., Mucciarelli A., Dalessandro E., Ferraro F. R., Lanzoni B., 2013a, ApJ, 778, 64
Lovisi L., Mucciarelli A., Lanzoni B., Ferraro F. R., Dalessandro E., Monaco L., 2013b, ApJ, 772, 148
McWilliam A., 1998, AJ, 115, 1640
Mathys G., 1990, A&A, 232, 151
Murphy S. J., Shibahashi H., 2015, MNRAS, 450, 4475
Murphy S. J., Bedding T. R., Shibahashi H., Kurtz D. W., Kjeldsen H., 2014, MNRAS, 441, 2515
Murphy S. J. et al., 2015, Publ. Astron. Soc. Aust., 32, e036
Murphy S. J., Fossati L., Bedding T. R., Saio H., Kurtz D. W., Grassitelli L., Wang E. S., 2016, MNRAS, 459, 1201
Niemczura E. et al., 2015, MNRAS, 450, 2764
Noguchi K. et al., 2002, PASJ, 54, 855
Paunzen E., Andrievsky S. M., Chernyshova I. V., Klochkova V. G., Panchuk V. E., Handler G., 1999, A&A, 351, 981
Paxton B. et al., 2013, ApJS, 208, 4
Ryabchikova T., Nesvacil N., Weiss W. W., Kochukhov O., Stütz C., 2004, A&A, 423, 705
Saio H., Kurtz D. W., Takata M., Shibahashi H., Murphy S. J., Sekii T., Bedding T. R., 2015, MNRAS, 447, 3264
Schmid V. S., Aerts C., 2016, A&A, 592, A116
Shibahashi H., Kurtz D. W., 2012, MNRAS, 422, 738
Sills A., Adams T., Davies M. B., 2005, MNRAS, 358, 716
Smith M. A., 1971, A&A, 11, 325
Stürenburg S., 1993, A&A, 277, 139
Stępień K., 2000, A&A, 353, 227
Takeda Y., Ohkubo M., Sadakane K., 2002, PASJ, 54, 451
Takeda Y., Ohkubo M., Sato B., Kambe E., Sadakane K., 2005, PASJ, 57, 27
Takeda Y., Sato B., Murata D., 2008, PASJ, 60, 781
Takeda Y., Kang D., Han I., Lee B., Kim K., Kawanomoto S., Ohishi N., 2012, PASJ, 64, 38
Westin J., Sneden C., Gustafsson B., Cowan J. J., 2000, ApJ, 530, 783

APPENDIX A: ATOMIC LINE DATA FOR Fe LINES

Table A1. Data for 67 Fe I lines selected for analysis. χ is the lower excitation potential.

Wavelength (Å)	χ (eV)	log gf	W_λ (mÅ)
4430.614	2.223	− 1.728	40.0
4442.338	2.198	− 1.228	65.0
4447.718	2.223	− 1.339	56.4
4489.739	0.121	− 3.899	6.0
4494.563	2.198	− 1.143	77.1
4602.940	1.485	− 2.208	30.3
4736.772	3.211	− 0.752	41.1
4872.136	2.882	− 0.567	60.6
4890.754	2.875	− 0.394	81.2
4891.492	2.851	− 0.111	103.2
4903.308	2.882	− 0.926	48.6
4918.993	2.865	− 0.342	79.0
4938.813	2.875	− 1.077	30.4
4946.385	3.368	− 1.010	12.7
4966.087	3.332	− 0.840	32.4
4973.101	3.960	− 0.850	18.8
4994.129	0.915	− 2.969	15.8
5014.941	3.943	− 0.270	43.0
5022.236	3.984	− 0.490	23.6
5049.819	2.279	− 1.355	49.9
5068.765	2.940	− 1.041	33.5
5074.748	4.220	− 0.160	41.9
5083.338	0.958	− 2.842	16.5
5090.767	4.256	− 0.360	17.9
5123.719	1.011	− 3.057	14.1
5133.681	4.178	0.200	60.2
5162.292	4.178	0.020	59.3
5192.343	2.998	− 0.421	73.0
5198.711	2.223	− 2.140	15.5
5216.274	1.608	− 2.082	31.8
5232.939	2.940	− 0.057	101.4
5242.491	3.634	− 0.970	17.2
5266.555	2.998	− 0.385	77.2
5281.790	3.038	− 0.833	43.8
5283.621	3.241	− 0.524	56.4
5339.928	3.266	− 0.720	40.0
5364.858	4.446	0.230	46.2
5367.479	4.415	0.440	55.2
5369.958	4.371	0.536	64.4
5383.369	4.312	0.645	76.9
5389.479	4.415	− 0.410	17.1
5393.167	3.241	− 0.715	38.7
5400.502	4.371	− 0.100	32.3
5405.774	0.990	− 1.852	84.9

Table A1 – *continued*

Wavelength (Å)	χ (eV)	log gf	W_λ (mÅ)
5410.910	4.473	0.400	49.4
5424.069	4.320	0.520	83.8
5434.523	1.011	− 2.126	66.6
5445.042	4.386	0.040	39.8
5446.916	0.990	− 1.910	94.3
5569.618	3.417	− 0.500	44.4
5572.841	3.396	− 0.275	59.6
5576.090	3.430	− 0.900	23.5
5586.756	3.368	− 0.096	72.7
6020.170	4.607	− 0.210	17.7
6024.049	4.548	− 0.060	30.9
6136.615	2.453	− 1.410	45.6
6137.694	2.588	− 1.346	36.8
6213.429	2.223	− 2.481	3.7
6219.279	2.198	− 2.448	6.0
6230.726	2.559	− 1.276	51.0
6252.554	2.404	− 1.767	30.5
6265.131	2.176	− 2.550	7.2
6301.498	3.654	− 0.718	35.1
6393.602	2.433	− 1.576	28.7
6400.000	3.602	− 0.290	53.3
6421.349	2.279	− 2.014	13.2
6592.913	2.727	− 1.470	21.5

Table A2. Data for 21 Fe II lines selected for analysis.

Wavelength (Å)	χ (eV)	log gf	W_λ (mÅ)
4416.830	2.778	− 2.580	96.9
4491.405	2.855	− 2.590	69.6
4508.288	2.855	− 2.318	110.3
4515.339	2.844	− 2.422	88.2
4520.224	2.807	− 2.590	86.4
4541.524	2.855	− 3.030	74.0
4576.340	2.844	− 2.920	63.1
4620.521	2.828	− 3.226	30.5
4993.358	2.807	− 3.650	15.8
5197.577	3.230	− 2.167	90.0
5234.625	3.221	− 2.268	94.7
5264.812	3.230	− 3.108	29.7
5276.002	3.199	− 1.963	85.0
5284.109	2.891	− 3.010	42.2
5325.553	3.221	− 3.210	22.3
5425.257	3.199	− 3.210	18.6
5534.847	3.245	− 2.770	49.3
6084.111	3.199	− 3.791	6.4
6149.258	3.889	− 2.720	17.5
6247.557	3.892	− 2.340	39.6
6432.680	2.891	− 3.580	17.7

APPENDIX B: DATA FOR EACH ELEMENT AND LINE

Table B1. Atomic data, W_λ, and the abundances derived from each line of detected elements together with the number (N) of lines and average abundance with standard deviation.

Ion/code	Wavelength (Å)	χ (eV)	$\log gf$	W_λ (mÅ)	$\log X$	Remark
Li I	$N = 1$				≤ 1.38	
3.00	6707.773	0.000	0.002	≤ 0.4	≤ 1.38	Single line
C I	$N = 10$				7.82 ± 0.15	
6.00	4770.027	7.483	-2.439	8.3	8.03	
6.00	4932.049	7.685	-1.658	24.4	7.91	
6.00	5052.167	7.685	-1.304	42.2	7.85	
6.00	5380.337	7.685	-1.615	24.4	7.87	
6.00	6013.166	8.647	-1.370	11.8	7.60	Doublet fit
6.00	6014.830	8.643	-1.710	4.4	7.84	
6.00	7111.472	8.640	-1.086	8.5	7.54	
6.00	7113.178	8.647	-0.774	20.7	7.66	
6.00	7115.172	8.643	-0.935	26.9	7.87	Doublet fit
6.00	7116.991	8.647	-0.907	29.5	7.98	
O I	$N = 3$				8.38 ± 0.09	
8.00	6155.961	10.740	-1.363	6.9	8.51	Triplet fit
8.00	6156.737	10.740	-1.488	11.7	8.31	Triplet fit
8.00	6158.149	10.741	-1.841	14.3	8.32	Triplet fit
Na I	$N = 4$				5.75 ± 0.04	
11.00	5682.633	2.102	-0.700	20.8	5.81	
11.00	5688.194	2.104	-1.400	31.4	5.73	Doublet fit
11.00	6154.226	2.102	-1.560	2.8	5.74	
11.00	6160.747	2.104	-1.260	5.2	5.71	
Mg I	$N = 3$				7.13 ± 0.04	
12.00	4571.096	0.000	-5.691	5.7	7.10	
12.00	4730.029	4.346	-2.523	6.2	7.19	
12.00	5711.088	4.346	-1.833	23.0	7.11	
Mg II	$N = 1$				7.29	
12.01	4481.126	8.863	0.730	292.7	7.29	Triplet fit
Si I	$N = 14$				7.05 ± 0.22	
14.00	5665.555	4.920	-2.040	4.0	7.01	
14.00	5675.417	5.619	-1.030	10.5	6.94	
14.00	5675.756	5.619	-1.780	4.2	7.28	
14.00	5684.484	4.954	-1.650	15.3	7.26	
14.00	5690.425	4.930	-1.870	8.0	7.16	
14.00	5948.541	5.082	-1.230	24.0	7.16	
14.00	6091.919	5.871	-1.400	4.9	7.15	
14.00	6155.134	5.619	-0.400	25.7	6.76	
14.00	6243.815	5.616	-0.770	11.1	6.71	
14.00	6244.466	5.616	-0.690	11.8	6.66	
14.00	6254.188	5.619	-0.600	25.3	6.95	
14.00	6721.848	5.862	-1.490	7.2	7.41	
14.00	7003.569	5.964	-0.970	12.1	7.19	
14.00	7034.901	5.871	-0.880	13.8	7.10	
Si II	$N = 3$				7.03 ± 0.07	
14.01	5957.559	10.066	-0.349	3.2	6.93	
14.01	5978.930	10.074	-0.061	8.4	7.10	
14.01	6347.109	8.121	0.297	104.3	7.07	
S I	$N = 8$				6.87 ± 0.08	
16.00	4694.113	6.524	-1.770	9.1	6.91	
16.00	4695.443	6.524	-1.920	6.1	6.88	

Table B1 – *continued*

Ion/Code	Wavelength (Å)	χ (eV)	log gf	W_λ (mÅ)	log X	Remark
16.00	4696.252	6.524	− 2.140	5.0	7.01	
16.00	6045.954	7.867	− 1.820	7.1	6.83	Triplet fit
16.00	6052.583	7.870	− 1.330	9.2	6.77	Doublet fit
16.00	6743.440	7.866	− 1.270	10.0	6.74	Triplet fit
16.00	6748.573	7.867	− 1.390	20.0	6.95	Triplet fit
16.00	6756.851	7.870	− 1.760	26.1	6.85	Triplet fit
Ca I	N = 25				5.95 ± 0.12	
20.00	4425.437	1.879	− 0.385	82.2	6.01	
20.00	4434.957	1.886	− 0.029	116.5	6.09	
20.00	4435.679	1.886	− 0.500	77.0	6.07	
20.00	4454.779	1.899	0.252	132.8	6.05	
20.00	4455.887	1.899	− 0.510	64.3	5.93	
20.00	4526.928	2.709	− 0.430	25.9	5.87	
20.00	5261.704	2.521	− 0.730	28.8	6.07	
20.00	5265.556	2.523	− 0.260	55.2	6.00	
20.00	5581.965	2.523	− 0.710	32.8	6.12	
20.00	5588.749	2.526	0.210	93.1	6.01	
20.00	5590.114	2.521	− 0.710	30.7	6.08	
20.00	5594.462	2.523	− 0.050	74.2	6.03	
20.00	5601.277	2.526	− 0.690	35.8	6.15	
20.00	5857.451	2.932	0.230	65.5	5.94	
20.00	6102.723	1.879	− 0.890	46.4	6.01	
20.00	6122.217	1.886	− 0.409	90.2	6.08	
20.00	6162.173	1.899	0.100	105.9	5.77	
20.00	6166.439	2.521	− 0.900	11.2	5.74	
20.00	6169.042	2.523	− 0.550	24.7	5.79	
20.00	6169.563	2.526	− 0.270	37.3	5.74	
20.00	6439.075	2.526	0.470	105.0	5.88	
20.00	6462.567	2.523	0.310	88.1	5.82	
20.00	6471.662	2.526	− 0.590	23.8	5.81	
20.00	6493.781	2.521	0.140	75.4	5.84	
20.00	6717.681	2.709	− 0.610	24.4	5.97	
Ca II	N = 3				6.02 ± 0.09	
20.01	5001.479	7.505	− 0.517	20.7	5.91	
20.01	5019.971	7.515	− 0.257	40.4	6.02	
20.01	5285.266	7.505	− 1.153	8.6	6.13	
Sc II	N = 9				2.8 ± 0.15	
21.01	4400.389	0.605	− 0.510	82.8	2.84	HfS fit
21.01	4415.557	0.595	− 0.640	98.5	2.97	HfS fit
21.01	5031.021	1.357	− 0.260	45.9	2.58	HfS fit
21.01	5526.790	1.768	0.130	66.9	2.75	HfS fit
21.01	5641.001	1.500	− 1.040	14.0	2.80	
21.01	5667.149	1.500	− 1.240	10.1	2.85	
21.01	5684.202	1.507	− 1.050	14.6	2.84	
21.01	6245.637	1.507	− 0.980	9.1	2.52	
21.01	6604.601	1.357	− 1.480	11.7	3.02	
Ti I	N = 15				4.59 ± 0.11	
22.00	4449.143	1.887	0.500	9.5	4.69	
22.00	4518.023	0.826	− 0.325	5.7	4.49	
22.00	4534.778	0.836	0.280	24.5	4.58	
22.00	4548.765	0.826	− 0.354	7.7	4.65	
22.00	4681.908	0.048	− 1.071	6.1	4.66	
22.00	4759.272	2.256	0.514	3.9	4.53	
22.00	4981.732	0.848	0.504	34.8	4.54	
22.00	4999.504	0.826	0.250	27.5	4.64	
22.00	5022.871	0.826	− 0.434	3.8	4.38	
22.00	5036.468	1.443	0.130	10.9	4.76	
22.00	5173.742	0.000	− 1.118	4.6	4.52	
22.00	5192.969	0.021	− 1.006	7.0	4.61	
22.00	5210.386	0.048	− 0.884	7.0	4.51	

Table B1 – *continued*

Ion/Code	Wavelength (Å)	χ (eV)	log *gf*	W_λ (mÅ)	log X	Remark
22.00	6258.104	1.443	− 0.355	3.2	4.65	
22.00	6258.709	1.460	− 0.240	6.3	4.85	
Ti II	N = 32				4.59 ± 0.18	
22.01	4409.243	1.243	− 2.638	15.8	4.71	
22.01	4409.516	1.231	− 2.569	15.1	4.60	
22.01	4411.925	1.224	− 2.520	10.5	4.38	
22.01	4421.938	2.061	− 1.770	29.9	4.78	
22.01	4444.558	1.116	− 2.030	40.8	4.50	
22.01	4450.482	1.084	− 1.450	104.1	4.69	
22.01	4464.450	1.161	− 2.080	72.8	4.99	
22.01	4470.857	1.165	− 2.280	37.8	4.74	
22.01	4488.331	3.123	− 0.820	51.8	4.96	
22.01	4441.734	1.180	− 2.410	30.3	4.76	
22.01	4518.327	1.080	− 2.555	14.9	4.46	
22.01	4529.474	1.572	− 2.030	50.7	4.98	
22.01	4544.028	1.243	− 2.400	16.8	4.48	
22.01	4568.314	1.224	− 2.650	7.1	4.31	
22.01	4708.665	1.237	− 2.340	21.6	4.53	
22.01	4764.526	1.237	− 2.950	10.4	4.79	
22.01	4779.985	2.048	− 1.370	49.3	4.65	
22.01	4798.521	1.080	− 2.430	15.5	4.34	
22.01	4805.085	2.061	− 1.100	77.4	4.74	
22.01	4911.193	3.123	− 0.340	36.3	4.24	
22.01	5010.212	3.095	− 1.290	12.3	4.60	
22.01	5013.677	1.582	− 1.935	24.0	4.43	
22.01	5129.152	1.892	− 1.390	62.4	4.69	
22.01	5154.070	1.566	− 1.750	42.0	4.53	
22.01	5185.913	1.893	− 1.350	50.9	4.50	
22.01	5211.536	2.590	− 1.356	16.1	4.40	
22.01	5336.786	1.582	− 1.590	56.3	4.57	
22.01	5381.021	1.566	− 1.920	30.5	4.51	
22.01	5418.764	1.582	− 2.000	24.6	4.48	
22.01	5490.690	1.566	− 2.650	7.3	4.53	
22.01	6491.561	2.061	− 1.793	18.1	4.45	
22.01	6998.905	3.123	− 1.453	11.3	4.68	
Cr I	N = 14				4.9 ± 0.11	
24.00	4545.953	0.941	− 1.370	8.6	5.07	
24.00	4616.120	0.983	− 1.190	4.9	4.66	
24.00	4626.174	0.968	− 1.320	5.8	4.85	
24.00	4646.162	1.030	− 0.700	21.6	4.9	
24.00	4651.282	0.983	− 1.460	3.8	4.81	
24.00	4652.152	1.004	− 1.030	9.4	4.81	
24.00	4718.426	3.195	0.090	5.8	5.09	
24.00	5204.506	0.941	− 0.208	62.0	4.95	
24.00	5206.038	0.941	0.019	80.3	4.95	
24.00	5296.691	0.983	− 1.400	6.0	4.92	
24.00	5297.376	2.899	0.167	9.0	4.97	
24.00	5298.277	0.983	− 1.150	8.9	4.85	
24.00	5348.312	1.004	− 1.290	8.9	5.01	
24.00	6978.488	3.463	0.142	2.5	4.81	
Cr II	N = 21				4.96 ± 0.12	
24.01	4558.650	4.073	− 0.410	68.9	4.70	
24.01	4592.049	4.073	− 1.217	22.3	4.79	
24.01	4616.629	4.072	− 1.291	22.3	4.86	
24.01	4618.803	4.073	− 0.860	56.6	4.99	
24.01	4634.070	4.072	− 0.990	42.5	4.92	
24.01	4812.337	3.864	− 1.995	11.5	5.09	
24.01	4824.127	3.871	− 0.970	67.0	5.10	
24.01	4836.229	3.858	− 2.000	11.5	5.12	
24.01	4848.235	3.864	− 1.140	43.3	5.06	
24.01	4884.607	3.858	− 2.080	6.3	4.93	

Table B1 – *continued*

Ion/Code	Wavelength (Å)	χ (eV)	log gf	W_λ (mÅ)	log X	Remark
24.01	5237.329	4.073	− 1.160	40.4	5.04	
24.01	5246.768	3.713	− 2.450	3.2	4.82	
24.01	5305.853	3.827	− 2.080	7.9	4.94	
24.01	5308.440	4.071	− 1.810	6.1	4.73	
24.01	5313.590	4.073	− 1.650	16.9	5.06	
24.01	5334.869	4.072	− 1.562	17.7	4.99	
24.01	5407.604	3.827	− 2.088	7.6	4.93	
24.01	5420.922	3.758	− 2.360	5.0	4.96	
24.01	5502.067	4.168	− 1.990	7.1	5.05	
24.01	5508.606	4.156	− 2.110	6.6	5.13	
24.01	5510.702	3.827	− 2.452	3.6	4.95	
Mn I	$N = 7$				4.57 ± 0.05	
25.00	4709.712	2.888	− 0.340	4.5	4.64	
25.00	4754.042	2.282	− 0.086	16.4	4.53	
25.00	4765.846	2.941	− 0.080	7.0	4.61	
25.00	4766.418	2.920	0.100	10.8	4.62	
25.00	4783.427	2.298	0.042	24.0	4.58	HfS fit
25.00	4823.524	2.319	0.144	26.6	4.50	HfS fit
25.00	6021.79	3.075	0.034	6.6	4.53	
Ni I	$N = 41$				5.7 ± 0.10	
28.00	4648.646	3.419	− 0.100	19.9	5.52	
28.00	4686.207	3.597	− 0.580	7.1	5.63	
28.00	4703.803	3.658	− 0.735	6.1	5.76	
28.00	4714.408	3.380	0.260	52.5	5.69	
28.00	4715.757	3.543	− 0.320	12.8	5.61	
28.00	4732.456	4.105	− 0.550	4.8	5.80	
28.00	4756.510	3.480	− 0.270	17.0	5.65	
28.00	4786.531	3.419	− 0.160	25.6	5.71	
28.00	4829.016	3.542	− 0.330	13.6	5.67	
28.00	4873.438	3.699	− 0.380	7.3	5.65	
28.00	4904.407	3.542	− 0.170	21.3	5.72	
28.00	4918.362	3.841	− 0.240	11.6	5.70	
28.00	4925.559	3.655	− 0.770	5.1	5.71	
28.00	4935.831	3.941	− 0.350	11.2	5.86	
28.00	4937.341	3.606	− 0.390	9.6	5.58	
28.00	4953.200	3.740	− 0.580	5.6	5.62	
28.00	4965.166	3.796	− 0.753	7.0	5.94	
28.00	4980.166	3.606	0.070	26.8	5.63	
28.00	5000.338	3.635	− 0.430	14.0	5.82	
28.00	5010.934	3.635	− 0.870	3.7	5.65	
28.00	5017.568	3.539	− 0.020	24.4	5.62	
28.00	5035.357	3.635	0.290	37.2	5.61	
28.00	5042.182	3.658	− 0.580	7.2	5.67	
28.00	5048.843	3.847	− 0.380	6.2	5.54	
28.00	5080.528	3.655	0.330	42.8	5.67	
28.00	5081.107	3.847	0.300	32.4	5.68	
28.00	5082.339	3.658	− 0.540	7.3	5.64	
28.00	5084.089	3.678	0.030	26.1	5.69	
28.00	5099.927	3.678	− 0.100	29.1	5.89	
28.00	5115.389	3.834	− 0.110	18.1	5.77	
28.00	5146.480	3.706	0.120	22.2	5.55	
28.00	5155.762	3.898	− 0.090	14.5	5.68	
28.00	5176.559	3.898	− 0.440	5.4	5.57	
28.00	5614.768	4.153	− 0.508	4.3	5.71	
28.00	5682.198	4.105	− 0.470	7.2	5.87	
28.00	6086.276	4.266	− 0.530	4.1	5.79	
28.00	6176.807	4.088	− 0.260	7.3	5.65	
28.00	6191.171	1.676	− 2.353	4.4	5.69	
28.00	6643.629	1.676	− 2.300	4.8	5.67	
28.00	6767.768	1.826	− 2.170	7.3	5.84	
28.00	6772.313	3.658	− 0.980	4.4	5.81	

Table B1 *– continued*

Ion/Code	Wavelength (Å)	χ (eV)	log gf	W_λ (mÅ)	log X	Remark
Cu I	$N = 2$				3.56 ± 0.05	
29.00	5105.537	1.389	-1.516	3.8	3.51	
29.00	5218.197	3.817	0.476	7.0	3.60	
Zn I	$N = 3$				4.15 ± 0.03	
30.00	4680.134	4.006	-0.815	8.1	4.11	
30.00	4722.153	4.030	-0.338	23.7	4.17	
30.00	4810.528	4.078	-0.137	32.2	4.18	
Y II	$N = 7$				1.87 ± 0.06	
39.01	4883.684	1.084	0.070	39.6	1.88	
39.01	5087.416	1.084	-0.170	29.8	1.90	
39.01	5123.211	0.992	-0.830	7.9	1.84	
39.01	5200.406	0.992	-0.570	12.6	1.79	
39.01	5402.774	1.839	-0.510	4.3	1.88	
39.01	5509.895	0.992	-1.010	5.1	1.80	
39.01	5662.925	1.944	0.160	19.2	1.98	
Zr II	$N = 1$				2.38	
40.01	5112.297	1.665	-0.590	5.0	2.38	
Ba II	$N = 4$				1.58 ± 0.04	
56.01	4553.995	0.000	0.163	131.1	1.52	HfS fit
56.01	4934.076	0.000	-0.150	113.8	1.58	HfS fit
56.01	5853.668	0.604	-1.000	21.6	1.62	HfS fit
56.01	6141.713	0.704	-0.076	70.8	1.60	HfS fit
Ce II	$N = 1$				1.26	
58.01	4628.161	0.516	0.008	2.2	1.26	
Nd II	$N = 1$				0.91	
60.01	5130.586	1.304	0.570	1.4	0.91	

This paper has been typeset from a TEX/LATEX file prepared by the author.